

ORIGINAL ARTICLE

Plasmonic enhancement and polarization dependence of nonlinear upconversion emissions from single gold nanorod@SiO₂@CaF₂:Yb³⁺,Er³⁺ hybrid core-shell-satellite nanostructures

Jijun He¹, Wei Zheng², Filip Ligmajer³, Chi-Fai Chan⁴, Zhiyong Bao¹, Ka-Leung Wong⁴, Xueyuan Chen², Jianhua Hao¹, Jiyan Dai¹, Siu-Fung Yu¹ and Dang Yuan Lei¹

Lanthanide-doped upconversion nanocrystals (UCNCs) have recently become an attractive nonlinear fluorescence material for use in bioimaging because of their tunable spectral characteristics and exceptional photostability. Plasmonic materials are often introduced into the vicinity of UCNCs to increase their emission intensity by means of enlarging the absorption cross-section and accelerating the radiative decay rate. Moreover, plasmonic nanostructures (e.g., gold nanorods, GNRs) can also influence the polarization state of the UC fluorescence—an effect that is of fundamental importance for fluorescence polarization-based imaging methods yet has not been discussed previously. To study this effect, we synthesized GNR@SiO₂@CaF₂:Yb³⁺,Er³⁺ hybrid core-shell-satellite nanostructures with precise control over the thickness of the SiO₂ shell. We evaluated the shell thickness-dependent plasmonic enhancement of the emission intensity in ensemble and studied the plasmonic modulation of the emission polarization at the single-particle level. The hybrid plasmonic UC nanostructures with an optimal shell thickness exhibit an improved bioimaging performance compared with bare UCNCs, and we observed a polarized nature of the light at both UC emission bands, which stems from the relationship between the excitation polarization and GNR orientation. We used electrodynamic simulations combined with Förster resonance energy transfer theory to fully explain the observed effect. Our results provide extensive insights into how the coherent interaction between the emission dipoles of UCNCs and the plasmonic dipoles of the GNR determines the emission polarization state in various situations and thus open the way to the accurate control of the UC emission anisotropy for a wide range of bioimaging and biosensing applications.

Light: Science & Applications (2017) 6, e16217; doi:10.1038/lsa.2016.217; published online 19 May 2017

Keywords: Förster resonance energy transfer; gold nanorods; lanthanide-doped upconversion nanocrystals; plasmon-enhanced nonlinear fluorescence; polarization modulation

INTRODUCTION

Lanthanide-doped upconversion nanocrystals (UCNCs), which can absorb low-energy photons and emit high-energy photons by an anti-Stokes process^{1–3}, show great promise for numerous applications ranging from bioimaging^{4,5} and photothermal therapy^{6,7} to solar cells^{8,9}. Compared with conventional fluorescent materials such as organic dyes or quantum dots, lanthanide-doped UCNCs exhibit some unique properties, including excellent photostability, narrow and tunable emission bands, long luminescence lifetimes and relatively low cytotoxicity. Furthermore, their near-infrared excitation band is located in the so-called ‘biological transparency window’, thus promising high-penetration depth and low-photothermal damage in biological tissues². However, UCNCs often suffer from low-emission

efficiency due to several factors such as structural defects, the small absorption cross-sections of the activator ions and the intrinsic nature of the anti-Stokes emission^{10,11}.

Many chemical and physical methods have been developed to enhance the emission efficiency of UCNCs, including host lattice manipulation^{12,13}, surface passivation^{14–17}, energy transfer modulation^{18–20} and the plasmonic enhancement effect^{21–34}. Using the last approach, the UC luminescence efficiency is highly increased by coupling UCNCs with localized surface plasmon resonances (LSPRs)—collective oscillations of free electrons in metal nanoparticles such as gold nanospheres or gold nanorods (GNRs). The two possible mechanisms of plasmon-enhanced UC luminescence can be simply summarized as follows. First, the plasmon-enhanced local

¹Department of Applied Physics, The Hong Kong Polytechnic University, Hong Kong, China; ²Key Laboratory of Optoelectronic Materials Chemistry and Physics, Fujian Institute of Research on the Structure of Matter, Chinese Academy of Sciences, Fuzhou, Fujian 350002, China; ³Central European Institute of Technology, Brno University of Technology, Brno 61669, Czech Republic and ⁴Department of Chemistry, Hong Kong Baptist University, Hong Kong, China
Correspondence: DY Lei, Email: dylei@polyu.edu.hk

Received 23 February 2016; revised 31 August 2016; accepted 4 September 2016; accepted article preview online 6 September 2016

electric field in the vicinity of the metal nanoparticles can increase the excitation rate of the lanthanide sensitizer ions (e.g., Yb^{3+}), which then absorb more near-infrared photons. Second, in the UC emission process, the radiative decay rate of the lanthanide activator ions (e.g., Er^{3+} , Tm^{3+} or Ho^{3+}) can also be increased by a plasmon-induced localized density of photonic states³⁵. Most of the previous studies on the coupling of UC luminescence and LSPR have focused on obtaining the highest possible intensity enhancement by means of harnessing both of these approaches^{23,24,26,29,36,37}. However, in the study by van Hulst and co-workers³⁸ on the closely related subject of plasmon-modulated fluorescence, it was established that it is not just the intensity of the emitted light that is modified by the LSPR but also its polarization state. So far, this aspect has been largely overlooked in studies on the plasmonic modulation of UC luminescence.

In the present work, we report the simultaneous luminescence intensity enhancement and polarization state modulation in $\text{GNR@SiO}_2\text{@CaF}_2\text{:Yb}^{3+},\text{Er}^{3+}$ (core-shell-satellite) hybrid nanostructures. First, the distance dependence of the plasmon-enhanced UC luminescence was investigated by gradually increasing the thickness of the silica spacer, and the advantage of the hybrid nanostructures was demonstrated in bioimaging experiments. Next, we examined the polarization state of the UC emissions from individual hybrid nanostructures. We found that the interaction between the two emission bands of the UCNCs and the two orthogonal plasmonic modes of the GNRs results in an extraordinary polarization state of the UC luminescence, which is controlled by the excitation polarization. We also performed comprehensive electrodynamic simulations to obtain a better understanding of the underlying physical mechanisms responsible for our experimental observations. By linking the results of experiments and simulations in the realm of Förster resonance energy transfer theory, we were able to fully explain how the spatial relationships between regions of enhanced electric field intensity and dipole orientations lead to the enhancement or suppression of UC emissions with a particular polarization state. To the best of our knowledge, this is the first work analyzing the plasmon-induced polarization state of the UC luminescence—a feature that is particularly important for the polarization-sensitive applications of fluorescence in diagnostics and imaging^{39–43}.

MATERIALS AND METHODS

Materials

Tetrachloroauric acid ($\text{HAuCl}_4\cdot 3\text{H}_2\text{O}$), sodium borohydride (NaBH_4), cetyltrimethyl ammonium bromide (CTAB), ascorbic acid (AA), silver nitrate (AgNO_3) and tetraethyl orthosilicate (TEOS) were purchased from Sigma-Aldrich (St. Louis, MO, United States). All chemicals were used without further treatment, and deionized water was used for all experiments.

Synthesis of the GNRs

The GNRs were synthesized according to the seed-mediated growth method⁴⁴. The seed solution was prepared by mixing 0.25 ml of 0.01 M HAuCl_4 with 9.75 ml of 0.1 M CTAB solution, and then 0.6 ml freshly prepared ice-cold aqueous solution of 0.01 M NaBH_4 was injected into it. After a 1 min rapid inversion, the seed solution was kept at room temperature for 2–5 h before use. Next, 2 ml of 0.01 M HAuCl_4 , 0.4 ml of 0.01 M AgNO_3 , 0.32 ml of 0.1 M AA, 0.8 ml of 1 M HCl and 40 ml 0.1 M CTAB were mixed to form the growth solution for GNRs. Finally, the growth was initiated by injecting 10 μl of the seed solution into the growth solution, and the solution was left undisturbed at room temperature for at least 6 h. The as-prepared GNRs have an ensemble longitudinal LSPR wavelength at 724 nm. By

adding 1.5 ml more 0.01 M HAuCl_4 , the longitudinal LSPR wavelength will be reduced to 655 nm through the anisotropic oxidation of the GNRs.

Synthesis of mesoporous silica coating on the GNRs

The GNR@SiO_2 nanostructures were obtained via a modified Stöber method⁴⁵. A total of 10 ml of as-synthesized GNRs were centrifuged once at 6500 r.p.m. for 20 min to remove the excess CTAB. The precipitate was re-dispersed into 10 ml of deionized water, and 100 μl of 0.1 M NaOH aqueous solution was added to adjust the pH of the solution to 10–11. Then, 25, 30, 40, 50 and 65 μl of 10 vol% TEOS methanol solution were, respectively, added under gentle stirring. The mixture solution was kept stirring for 12 h until the reactions were complete. The resultant hybrid nanostructures were washed twice at 5500 r.p.m. for 10 min to remove the CTAB and re-dispersed in water of the same volume.

Synthesis of $\text{CaF}_2\text{:Yb}^{3+},\text{Er}^{3+}$ NCs and attachment to GNRs

The synthesis procedures of the hybrid nanostructures were briefly described earlier⁴⁶. Monodisperse, sub-10 nm $\text{CaF}_2\text{:18% Yb}^{3+}, 2\% \text{Er}^{3+}$ NCs were synthesized through a sodium co-doping co-precipitation route with a subsequent acid-washing treatment. The detailed fabrication procedures can be found in our previous works^{47,48}. The GNR@SiO_2 showed a negative zeta potential of -24.8 mV, derived from the dissociation of silanols. The $\text{CaF}_2\text{:Yb}^{3+},\text{Er}^{3+}$ NCs were positively charged, with a zeta potential of $+49.7$ mV. Therefore, by mixing 0.2 ml of ligand-free UCNC solution with 3 ml of silica-coated GNR solution, the UCNCs were attached on the surface of the GNR@SiO_2 through electrostatic attraction after 10 h.

Cell incubation

Human cervical carcinoma HeLa cells were purchased from American Type Culture Collection (ATCC) (#CCL-185, ATCC, Manassas, VA, USA). The HeLa cells were cultured in Dulbecco's Modified Eagle Medium (DMEM) supplemented with 10% fetal bovine serum (FBS) 1% penicillin and streptomycin at 37 °C in the presence of 5% CO_2 . To apply the $\text{GNR@SiO}_2\text{@CaF}_2\text{:Yb}^{3+},\text{Er}^{3+}$ hybrid nanostructures for UC bioimaging, the HeLa cells were incubated in DMEM containing 1 $\mu\text{g ml}^{-1}$ of the hybrid nanostructures at 37 °C for 24 h under 5% CO_2 and then washed with PBS sufficiently to remove the excess hybrid nanostructures. A control sample was also prepared by applying bare $\text{CaF}_2\text{:Yb}^{3+},\text{Er}^{3+}$ NCs for the bioimaging.

In-vitro UC luminescence bioimaging

The bioimaging of the HeLa cells incubated with pristine $\text{CaF}_2\text{:Yb}^{3+},\text{Er}^{3+}$ NCs and hybrid $\text{GNR@SiO}_2\text{@CaF}_2\text{:Yb}^{3+},\text{Er}^{3+}$ nanostructures was performed on a commercial confocal laser scanning microscope. The samples were excited by a 980 nm wavelength laser, and two visible UC emission channels were detected in the green (500–600 nm) and red (600–700 nm) spectral regions.

Characterization

The morphological features of the pristine GNR@SiO_2 and $\text{GNR@SiO}_2\text{@CaF}_2\text{:Yb}^{3+},\text{Er}^{3+}$ hybrid nanostructures were characterized with a JEM-2100F field-emission transmission electron microscope (TEM) (JEOL USA, Peabody, MA, USA) operating at 300 kV and an upgraded JEOL JSM-633F field-emission scanning electron microscope (SEM) (JEOL USA, Peabody, MA, USA). The absorption spectra of the GNRs in water were measured with a Shimadzu UV2550 Spectrophotometer (Shimadzu Corporation, Kyoto, Japan). Zeta-potential measurements were carried out using a Malvern Zetasizer

3000 HAS (Malvern Instruments Ltd, Malvern, UK). The UC luminescence spectra of the pristine and hybrid UCNCs in the solution phase were collected on a UK Edinburgh Instruments FLS900 Fluorescence Spectrometer (Edinburgh Instruments Ltd, Livingston, UK) equipped with a CNI MDL-III-980 diode laser (Changchun New Industries Optoelectronics Tech. Co., Ltd, Changchun, China). Lifetime measurements were performed on a UK Edinburgh Instruments FLS900 Fluorescence Spectrometer with a time-correlated single-photon counting module, whereas a 980 nm pulse laser generated by a Continuum Panther EX optical parametric oscillator (Continuum located, San Jose, CA, USA) was used as the excitation source. The single-particle scattering and UC luminescence spectra of the individual nanostructures were recorded with a home-built, polarization-resolved dark-field microscope equipped with a CNI MDL-III-980 diode laser. All the measured spectra were corrected for the spectral sensitivity and polarization response of the system.

RESULTS AND DISCUSSION

The synthesis procedure of the $\text{GNR@SiO}_2\text{@CaF}_2\text{:Yb}^{3+},\text{Er}^{3+}$ core-shell-satellite nanostructures is illustrated in Figure 1a. First, CTAB-coated GNRs were grown in an aqueous solution using a seed-mediated method^{49,50}. It is well-known that GNRs exhibit two LSPR modes: a transverse one and a longitudinal one. The plasmon wavelength of the latter can be flexibly tuned across the whole visible and near-infrared region by precisely tailoring the aspect ratio of the GNRs⁵¹. To study the influence of the LSPR on the UC emission properties, here we tuned the transverse and longitudinal LSPR wavelengths of the GNRs to match the two emission bands of the $\text{CaF}_2\text{:Yb}^{3+},\text{Er}^{3+}$ NCs. The average length and diameter of the synthesized CTAB-coated GNRs that met these requirements were determined to be 82 ± 7 nm and 32 ± 3 nm, respectively (see TEM images in Figure 1c–1e and Supplementary Fig. S1). If the UCNCs were attached in direct contact with the GNRs, the excited activators could undergo nonradiative decay due to energy and possible charge transfer to the metal nanoparticles. This would result in a lower luminescence enhancement or even quenching. To avoid this undesired process and examine the distance-dependent plasmon-enhanced

UC luminescence, we synthesized several batches of GNRs covered with mesoporous silica spacers with several thicknesses (9, 15, 19, 23 and 35 nm) via a modified Stöber method (see TEM images in Figure 1c and 1d; Supplementary Fig. S1a–S1e)⁴⁵. After the silica coating, the longitudinal plasmon peak red-shifts by 10–30 nm due to the increased refractive index of the surrounding medium, as shown in Supplementary Fig. S2 (Ref. 44). The $\text{CaF}_2\text{:Yb}^{3+},\text{Er}^{3+}$ NCs were synthesized through a sodium co-doping co-precipitation route followed by an acid-washing treatment^{47,48}, which provides a solution of monodisperse, positively charged NCs with good water solubility^{47,52}. Their average diameter was determined to be 7.5 nm from a TEM analysis (see Figure 1b for a representative TEM micrograph). As silica in aqueous solution is typically negatively charged, the UCNCs can be easily attached onto the surface of the GNR@SiO_2 nanostructures through electrostatic attraction⁵³. The TEM images in Figure 1e and Supplementary Fig. S1f–S1h show that the $\text{GNR@SiO}_2\text{@CaF}_2\text{:Yb}^{3+},\text{Er}^{3+}$ hybrid nanostructures were successfully formed after the simple mixing of the two constituent solutions. A detailed TEM analysis showed that nearly all the GNR@SiO_2 nanoparticles were attached to a certain number of UCNCs, and approximately 50% of the UCNCs were left unbound.

The UC luminescence was measured using illumination by a 980-nm continuous wave diode laser with a power density of ~ 10 W cm^{-2} . Figure 2a shows that the emission spectrum of the bare $\text{CaF}_2\text{:Yb}^{3+},\text{Er}^{3+}$ NCs exhibits two emission bands centered at 540 nm (green) and 660 nm (red), which correspond to the $^2\text{H}_{11/2}, ^4\text{S}_{3/2} \rightarrow ^4\text{I}_{15/2}$ and $^4\text{F}_{9/2} \rightarrow ^4\text{I}_{15/2}$ transitions of Er^{3+} ions, respectively (see the energy-level diagram in Supplementary Fig. S3)^{3,10}. Although the UC emission spectra of the $\text{GNR@SiO}_2\text{@CaF}_2\text{:Yb}^{3+},\text{Er}^{3+}$ hybrid nanostructures show the same spectral shape as the bare UCNCs, the emission intensity is strongly influenced by the distance between the GNRs and UCNCs (the silica shell thickness), as shown in Figure 2b. Figure 2c shows the extracted emission enhancement factor as a function of the silica shell thickness by calculating the ratio of the integrated emission intensities (510–570 nm for green emission and 630–680 nm for red emission) of each hybrid nanostructure and the

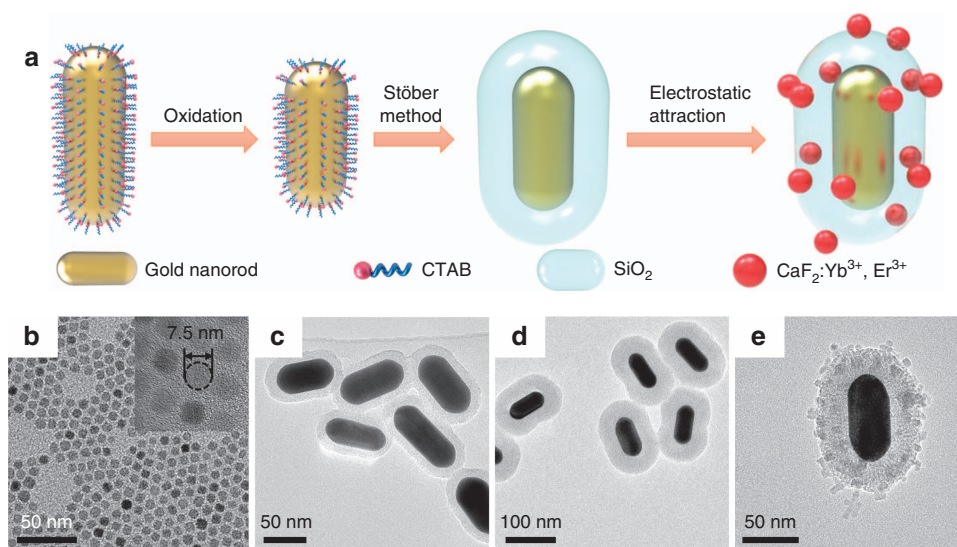


Figure 1 (a) Synthesis procedure of the $\text{GNR@SiO}_2\text{@CaF}_2\text{:Yb}^{3+},\text{Er}^{3+}$ hybrid nanostructures. CTAB-capped GNRs were oxidized to decrease their aspect ratio and obtain a suitable LSPR wavelength. In the next step, the GNRs were covered with a silica spacer, and the UCNCs were then attached to their surface by electrostatic attraction. (b–e) TEM images of **b** bare $\text{CaF}_2\text{:Yb}^{3+},\text{Er}^{3+}$ NCs, **c** GNR@SiO_2 (9 nm) nanostructures, **d** GNR@SiO_2 (35 nm) nanostructures and **e** GNR@SiO_2 (23 nm) $\text{@CaF}_2\text{:Yb}^{3+},\text{Er}^{3+}$ hybrid nanostructures.

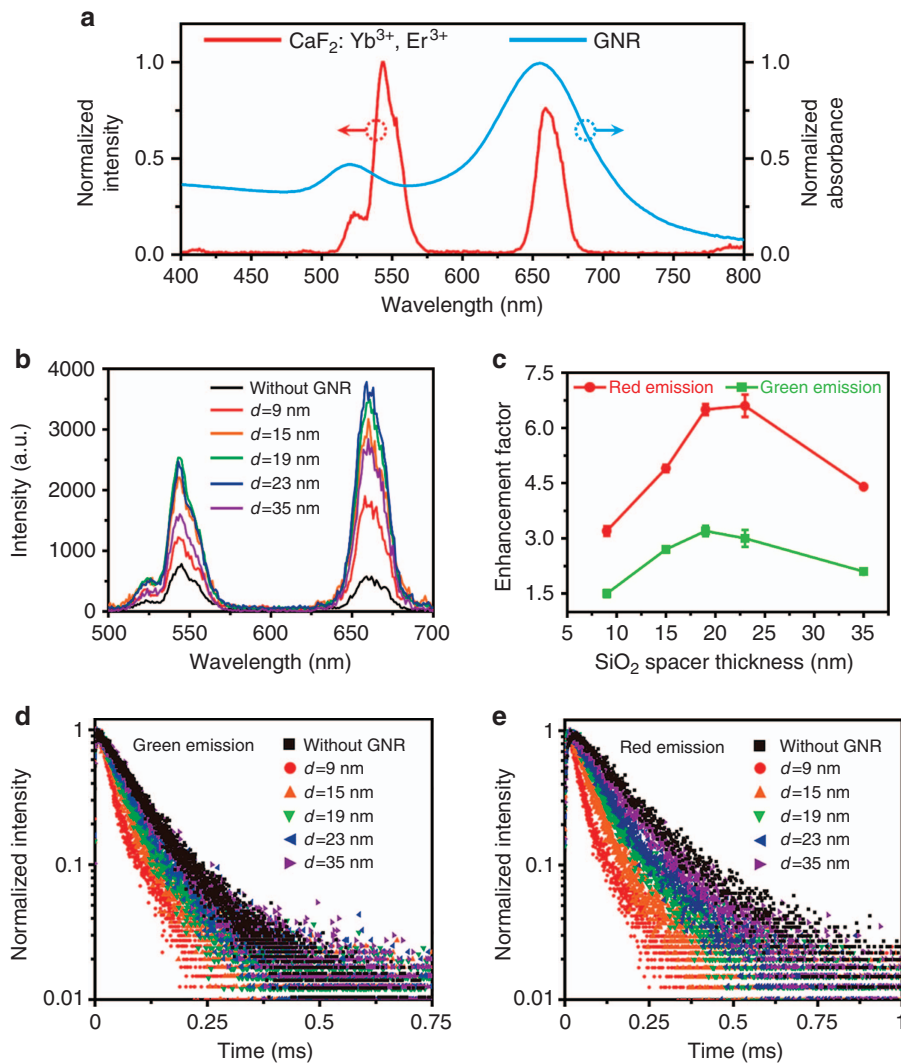


Figure 2 (a) Emission spectrum of bare $\text{CaF}_2\text{:Yb}^{3+}, \text{Er}^{3+}$ NCs (red) and absorbance spectrum of GNRs in water (blue). (b) Emission spectra of bare $\text{CaF}_2\text{:Yb}^{3+}, \text{Er}^{3+}$ NCs and $\text{GNR@SiO}_2\text{:CaF}_2\text{:Yb}^{3+}, \text{Er}^{3+}$ nanostructures with different silica spacer thicknesses (the concentration of UCNCs in all samples was fixed at 0.32 mg ml^{-1}). (c) Luminescence enhancement factors for both green and red emission bands as a function of the silica spacer thickness. The enhancement factors were extracted from the emission spectra shown in b. Error bars in the figure represent the standard deviation of three enhancement factors calculated for three measurements. (d, e) UC luminescence decay curves for the d green and e red emissions of $\text{GNR@SiO}_2\text{:CaF}_2\text{:Yb}^{3+}, \text{Er}^{3+}$ with different silica spacer thicknesses.

bare UCNCs. First, the intensity enhancement of both the green and red emission bands increases as the thickness of the silica spacer increases from 9 nm. When the spacer thickness reaches 19 nm, the enhancement factor of the green emission reaches its maximum value (3). However, the highest value of the red emission enhancement factor (6.7) is substantially larger than that of its green counterpart and occurs with a slightly thicker silica spacer (23 nm). Although the difference between the enhancement factors of the different UC emission bands has been reported by other groups, the enhancement factor of the green emission was usually the larger of the two^{22–24,29,54}. We ascribe this contradiction to the fact that in those works, the plasmonic materials of choice were metal nanospheres, which have only one plasmonic peak located near the green emission band of Er^{3+} ions, unlike the GNRs used in our experiment^{23,24,32,54}. It is natural that in those cases, the LSPR will have significant influence only on the green emission band. In our case, the stronger longitudinal plasmon resonance of the GNRs generates a larger enhancement factor for the

red emission than for the green emission. Note that the enhancement factor reported here could be significantly underestimated due to the presence of unbound UCNCs in the mixed solution and that the enhancement factor for the red emission band can be well above an order of magnitude on attaching all the UCNCs onto the GNR@SiO_2 .

To test the utility of the $\text{GNR@SiO}_2\text{:CaF}_2\text{:Yb}^{3+}, \text{Er}^{3+}$ hybrid nanostructures in biological imaging, we carried out a cellular imaging experiment with HeLa cells. The hybrid nanostructures with 19-nm thick silica shells were selected to be incubated with HeLa cells at 37 °C for 24 h under 5% CO_2 . Figure 3a–3d and Supplementary Fig. S4 show images of the live HeLa cells after incubation with the hybrid nanostructures captured at randomly selected sample areas with a laser scanning confocal multiphoton microscope. We recorded the UC luminescence of the hybrid nanostructures in both the green (500–600 nm, Figure 3b) and red emission (600–700 nm, Figure 3c) channels. An overlay of the green-channel, red-channel and bright-field images demonstrates that the hybrid nanostructures had crossed

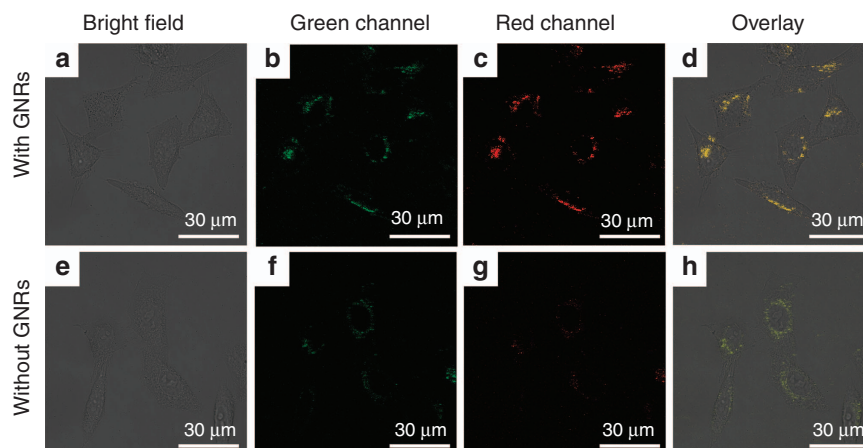


Figure 3 Confocal laser scanning microscopy images of HeLa cells incubated with GNR@SiO₂(19 nm)@CaF₂:Yb³⁺,Er³⁺ hybrid nanostructures (top row: **a**, bright field image; **b**, green channel image; **c**, red channel image and **d**, overlay imaging.) and CaF₂:Yb³⁺,Er³⁺ NCs (bottom row: **e**, bright field image; **f**, green channel image; **g**, red channel image and **h**, overlay imaging).

the cell membrane and accumulated in the cytoplasmic region. For comparison, a control cellular imaging experiment was carried out on HeLa cells incubated with bare CaF₂:Yb³⁺,Er³⁺ NCs. Under the same laser power, the UC luminescence intensity in the HeLa cells incubated with the bare UCNCs was lower than that in the cells incubated with the hybrid nanostructures. Our results demonstrate that the GNR@SiO₂@CaF₂:Yb³⁺,Er³⁺ hybrid nanostructures can be used as a promising nonlinear fluorescent probe for high-contrast bioimaging applications.

To further understand the interaction between the LSPR and UC luminescence, we measured the UC luminescence lifetimes of both GNR@SiO₂@CaF₂:Yb³⁺,Er³⁺ hybrid nanostructures and the bare CaF₂:Yb³⁺,Er³⁺ NCs. As shown in Figure 2d and 2e, the UC luminescence lifetimes of the hybrid nanostructures are significantly shorter than those of the bare UCNCs. For the thickest spacer in our experiments (35 nm), the lifetimes of both the green and red emissions are almost equal to those of the bare UCNCs (88.5 and 166.4 μs, respectively). As the thickness of the silica spacer decreases to 9 nm, the lifetimes of the two emissions reach minimum values of 39.4 and 51.3 μs, respectively. The calculation details of the UC luminescence lifetimes can be found in the Supplementary Information and Supplementary Fig. S5. This verifies the fact that—similar to the emission from plasmon-coupled fluorescence dyes—the GNRs introduce new (radiative and nonradiative) decay pathways into the emission process of the nearby UCNCs and thus reduce the luminescence lifetimes of the UCNCs⁵⁵.

Once we have understood the plasmonic enhancement properties of our hybrid nanostructures, we turn to inquire into the influences of the LSPR of the GNRs on the polarization states of the UC emissions and the relevant physical mechanisms. To that end, we studied both the scattering and fluorescence properties of the hybrid nanostructures at the single-particle level. The measurements were carried out using a home-built optical system that is adapted on the base of an Olympus BX51 optical microscope (Olympus Corporation, Tokyo, Japan) (for a scheme of our optical system, see Supplementary Fig. S6). A 100-W tungsten white-light lamp was employed as an excitation source for the dark-field scattering measurements, and a light beam of a CNI MDL-III-980 diode laser (980 nm, 1 W) was introduced into the light path by a dichroic mirror to excite the UC luminescence. The laser light was linearly polarized, and its polarization direction was precisely controlled using a 980 nm half-wave plate. Both the scattering and fluorescence signals of the individual nanostructures were collected by a

combination of an Acton SpectraPro 2300i spectrograph (Princeton Instruments, Trenton, NJ, USA) and a Princeton Instruments PIXIS 400 CCD (Princeton Instruments). During the measurement, a broad-band polarizer (hereafter called an analyzer) in front of the spectrograph was rotated at 30° per step to determine the polarization state of both the scattered light and the UC emissions. The samples were prepared by depositing GNR@SiO₂(19 nm)@CaF₂:Yb³⁺,Er³⁺ nanostructures on a glass slide at a surface number density of $\sim 3 \times 10^4 \text{ mm}^{-2}$. To verify the orientation of the observed hybrid nanostructures, the samples were subsequently imaged by SEM.

The correlated SEM and scattering images of the GNR@SiO₂@CaF₂:Yb³⁺,Er³⁺ hybrid nanostructures are shown in Figure 4a. The SEM analysis confirmed that every bright spot in the scattering image corresponds to a well-separated individual hybrid nanostructure. Figure 4b shows a representative dark-field scattering spectrum of a single hybrid nanostructure selected from the ensemble shown in Figure 4a (marked with a star), with a characteristic peak at 662 nm resulting from a longitudinal LSPR. A peak corresponding to the transverse LSPR does not manifest itself in the scattering spectrum, as it is much weaker than the longitudinal one⁵⁶. Figure 4c shows a polar plot of the scattering intensity of the same single nanostructure as a function of the analyzer angle. We can observe a typical dipole-like pattern, which is well-fitted by a cosine-squared function. For convenience, the zero analyzer angle is defined as parallel to the long axis of the GNR core (as shown in the inset of Figure 4a). To analyze the polarization state of the light quantitatively, a parameter called the degree of polarization (DOP) is defined as

$$\text{DOP} = \frac{I_{\max} - I_{\min}}{I_{\max} + I_{\min}} \quad (1)$$

where I_{\max} and I_{\min} are the maximum and minimum intensities in the polar plot, respectively (a totally polarized light has a DOP of 1, whereas an un-polarized light has a DOP of 0). In our case, the large DOP of the scattered light (0.92) arises from the inherently polarized longitudinal LSPR mode of the GNR core, which can be regarded as an electric dipole oscillating along the long axis of the GNR. The orientation of a particular hybrid nanostructure can thus be easily determined from its scattering polar plot without a need for verification by SEM imaging⁵⁷.

After the scattering measurement, we switched the optical system to fluorescence mode and measured the UC emission from the very same hybrid nanostructure (Figure 5). The UC emission spectra were

recorded as the angle of analyzer varied from 0 to 2π , whereas the polarization of the excitation laser was either parallel (Figure 5a) or perpendicular (Figure 5d) to the long axis of the hybrid nanostructure,

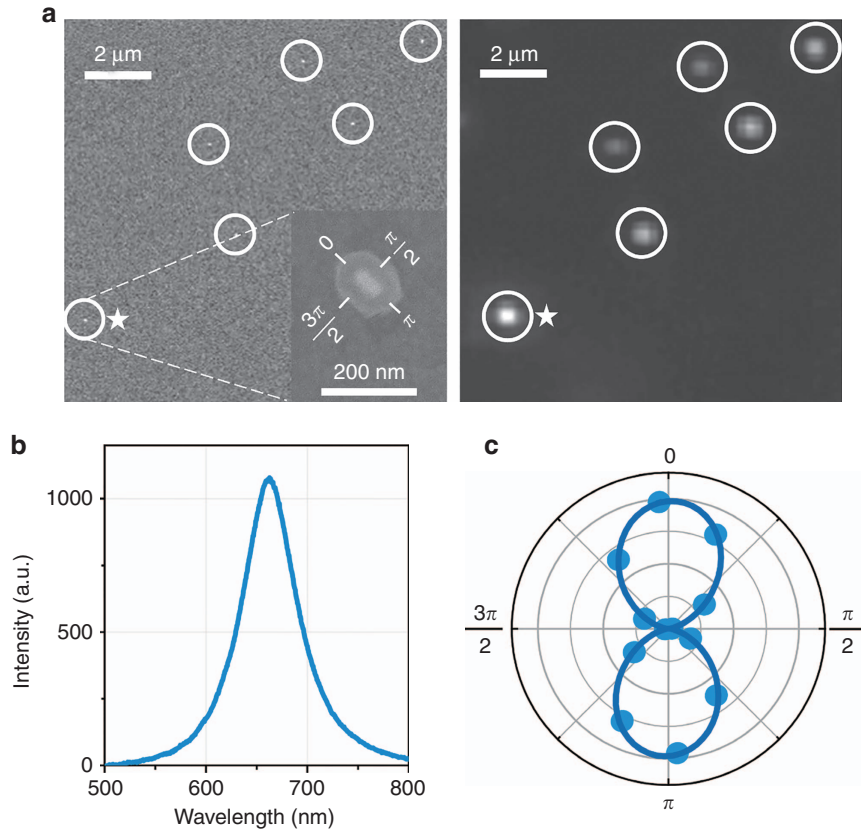


Figure 4 (a) Correlated SEM (left) and scattering (right) images of the GNR@SiO₂@CaF₂:Yb³⁺,Er³⁺ hybrid nanostructures. Each nanostructure is indicated by a circle. The inset of the SEM picture shows a selected single hybrid nanostructure that was used in the following experiments. (b) Scattering spectrum of the selected hybrid nanostructure. (c) Polar plots of the scattering intensity of the hybrid nanostructure as a function of the analyzer angle (the solid line corresponds to a cosine-squared fit of the experimental data). For convenience, we define the analyzer angle as shown in the inset of the SEM picture in a.

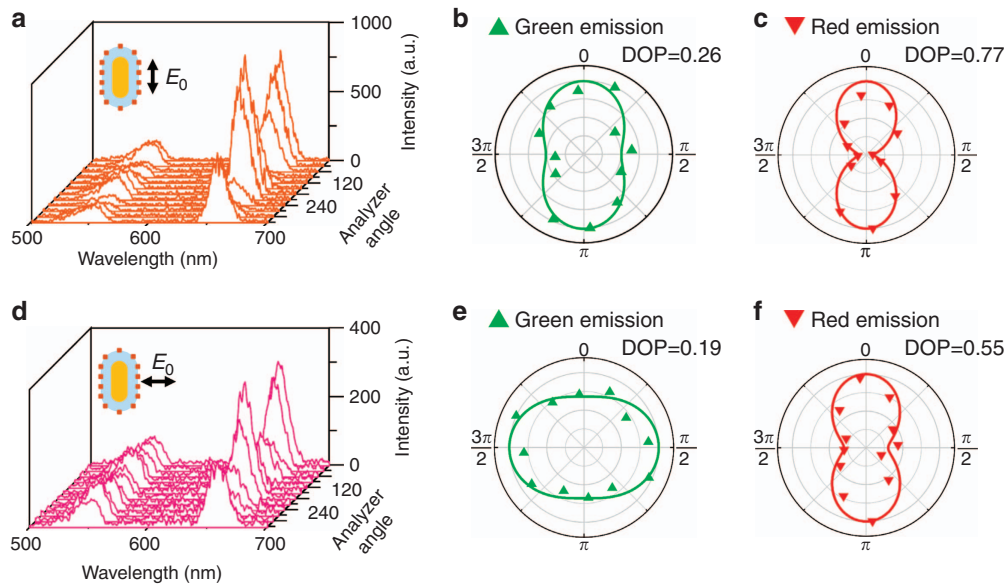


Figure 5 (a) UC emission spectra obtained as the analyzer angle varied from 0– 2π under excitation polarization parallel to the long axis of the hybrid nanostructure. From these spectra, the polar plots were extracted for the green (b) and red (c) emissions. (d) UC emission spectra under perpendicular excitation and corresponding polar plots for green (e) and red (f) emissions. The lines in the polar plots are cosine-squared fits of the experimental data. The calculated DOPs are shown in the top right corner of each polar plot.

and we observed in both cases that the emission intensities fluctuated periodically as the analyzer was rotated. These results clearly indicate that the UC luminescence became polarized when the UCNCs were in the vicinity of a GNR. To better visualize this polarization dependence in the spectra, we have extracted polar plots of the UC emission at green and red emission wavelengths (Figure 5b, 5e and 5c, 5f, respectively) and calculated the corresponding DOPs. For the case of the parallel excitation, both the green and red emissions follow the scattering polarization pattern of the GNR itself (Figure 4c), although the DOP of the green emission is slightly reduced. In the case of the perpendicular excitation, the red emission is still polarized along the long axis of the GNR like in the previous case, but surprisingly, the green emission pattern (again with somewhat lowered DOP) is now oriented in the direction perpendicular to the GNR long axis. The origins of the polarized UC emissions and their distinctly different polarization states will be described below in detail.

The emission polarization in an individual hybrid nanostructure can arise from two possible sources: one is the electromagnetic coupling between the GNR LSPR and the UC luminescence, and the other is the linearly polarized excitation⁵⁸. Let us first consider the emission polarization caused by the excitation laser. During an excitation process, when the incident electric field is parallel to the absorption dipole of a sensitizer ion (Yb^{3+}), the ion has the greatest chance to undergo an absorption process. Similarly, when the activator ion (Er^{3+}) has the same dipole orientation as the excited sensitizer, its prospect of obtaining the energy from the sensitizer is the highest. To identify the contribution of the excitation laser to the DOP of the UC luminescence, we prepared a sample with bare $\text{CaF}_2\text{:Yb}^{3+}, \text{Er}^{3+}$ NCs drop-casted onto a glass slide. The UC luminescence from a $5 \times 5 \mu\text{m}$ area of the glass slide was recorded (Supplementary Fig. S7), and the corresponding DOPs were calculated in the same manner as above. The DOPs for the green and red emissions of the UCNCs without GNRs are rather low, 0.11 and 0.10, respectively, and follow the polarization of the excitation laser. This indicates that although a linearly polarized excitation laser will impose its polarization on the UC emission, its contribution is not large enough to explain the total DOP that we have observed in the case of UCNCs in the vicinity of GNRs. The rest of the DOP must therefore be a result of the coupling between the LSPR and UC luminescence. To better understand the underlying physical mechanisms of this coupling, we performed a set of finite-difference time-domain calculations, which showed us how UCNCs located at different positions contribute to the overall emission in two different experimental situations.

A GNR (diameter 32 nm, length 82 nm) was modeled as a cylindrical body capped with two hemispheres, and the dielectric function of gold was modeled using the Drude–Lorentz dispersion model⁴⁴. The GNR was covered in a uniform silica layer with a thickness of 19 nm and a refractive index of 1.43. To verify that our model was correct, we calculated the extinction cross-section spectrum of the GNR@SiO₂ nanostructure in air (Supplementary Fig. S8). The pronounced longitudinal LSPR peak at 668 nm matches well with the one in our experiment (Figure 4b). It is also worthwhile to evaluate the electric field intensity distribution around the GNR@SiO₂ nanostructure, as the UC emission intensity is proportional to the square of the excitation power density²¹. Two maps of the excitation field enhancement were thus calculated—following the experimental conditions—under a linearly polarized 980-nm excitation source either parallel (Figure 6a) or perpendicular (Figure 6b) to the long axis of the GNR@SiO₂. In the case of parallel excitation, as high as an 8-fold intensity enhancement occurs on the silica surface due to the non-resonant excitation of the longitudinal localized surface plasmon of GNR, and the enhanced

electric field is mainly concentrated in regions around the tips of the GNR@SiO₂ (we refer to them as L-positions). When the excitation polarization is perpendicular to the long axis of the GNR@SiO₂, the regions with high intensity enhancement are now located along the sides of the GNR@SiO₂ (we refer to them as T-positions), and the maximum intensity enhancement is approximately threefold.

Because the emissions from the UCNCs located in the above-mentioned regions of high-electric field intensity will dominate the overall UC emission of the whole hybrid nanostructure, we will now investigate how this fact influences the polarization state of the emitted light. To this end, we calculated the emission properties of an activator ion, represented as a Hertzian dipole, that was placed at either the T- or L-position with its emission wavelength set at either 540 nm (green emission) or 660 nm (red emission), according to the corresponding experimental values. The GNR@SiO₂ nanostructure was located at the origin, and its orientation was along the Z axis (Figure 6c). Because we expect the activator ions in our hybrid nanostructures to be randomly oriented, we consider their emissions to be a linear combination of three dipoles oriented along the X, Y and Z axes. Following the experimental conditions, we evaluated the angular dependencies of the calculated emission intensities with respect to the polarization state in the far-field Y–Z plane (corresponding to the light collection by a microscope objective), and we present them in Figure 6d as normalized polar plots. When the dipole is located in position L, both the green and red emissions are highly polarized along the long axis of the GNR@SiO₂, closely resembling the behavior observed in the experiment (Figure 5b and 5c). For the dipole in position T, the simulated polar plot confirms that the radiation patterns of the green and red emissions are perpendicular to each other and have a decreased DOP. However, despite this remarkable agreement, these results still do not clarify the underlying physical mechanism of the polarized UC emissions.

To explain the results of our experiments and simulations, we need to find an effective theoretical model that can directly analyze the polarization properties of UC emissions. Selvin and co-workers⁵⁹ reported that the emission anisotropy from lanthanide ions could be evaluated by regarding them as electric dipoles and calculating the dipole–dipole interaction. However, their method cannot account for the plasmon-induced effect on the polarized emission from Er^{3+} because it is applicable only to studying the intrinsic emission anisotropy of lanthanide ions. Here, we analyzed the coupling between GNRs and UCNCs based on the mechanism proposed by Wang's group: an emitter can transfer its energy to a nearby GNR by exciting its LSPR⁵⁸. This energy transfer is attributed to a near-field interaction between the emission dipole of the UCNC and the plasmonic dipole of the GNR. Such a process can be characterized as a type of Förster resonance energy transfer (FRET), and its efficiency can be given by

$$\eta_{\text{ET}} = \frac{1}{1 + (r/R_0)^6} \quad (2)$$

where R_0 is the so-called Förster radius, and r is the distance between the activator and the GNR core. The Förster radius is the main characteristic of the interaction strength, and it is defined as the distance at which $\eta_{\text{ET}} = 50\%$ (so that a larger R_0 means that interaction will also happen at longer distances). The Förster radius can be further determined as

$$R_0^6 \propto \kappa^2 \int_0^\infty f_A(\lambda) \epsilon_G(\lambda) \lambda^4 d\lambda \quad (3)$$

where κ is an orientation factor that is determined by the orientations of the activator and the plasmonic dipole and the relative position between them, $f_A(\lambda)$ is the normalized activator emission spectrum,

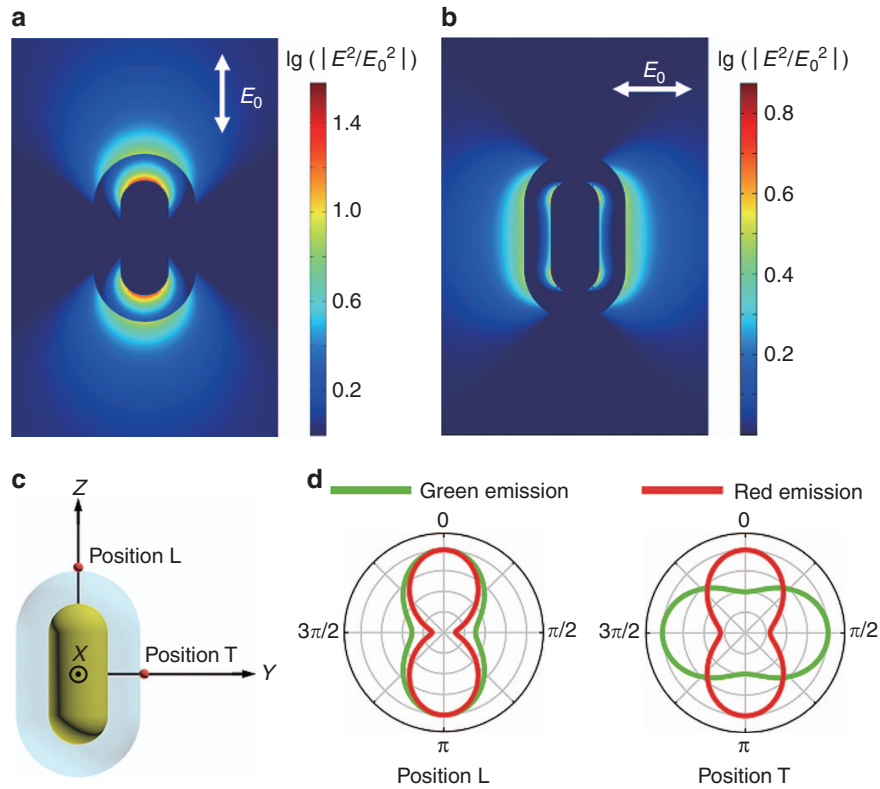


Figure 6 Calculated electric field intensity enhancement under a 980-nm excitation polarized parallel to (a) the long axis and (b) short axis of a single GNR@SiO₂ nanostructure. The enhancement factors are logarithmically scaled. (c) 3D diagram of GNR@SiO₂ with a dipole source placed at the two intersections of the silica surface with the coordinate axes Y and Z, indicated as positions T and L, respectively. (d) Polar plots of normalized calculated emission intensities of dipole sources with green (540 nm) and red (660 nm) emissions located at positions L and T.

and $\epsilon_G(\lambda)$ is the extinction spectrum of the GNR. From this equation, it follows that the FRET will occur only when there is an overlap between the $f_A(\lambda)$ and $\epsilon_G(\lambda)$. Keeping in mind the shapes of these spectra in our case (Figure 2a), this means that the green and red emissions will be modulated by the transverse and longitudinal plasmonic dipoles, respectively. To help us estimate the magnitudes of these interactions, we first calculated the FRET efficiency for the coupling between the red-emitter and the longitudinal plasmonic dipole using Equation (3) (details of the calculation in the Supplementary Information). As a consequence of the good spectral overlap, the efficiency is very high in this case, regardless of whether the emitter is located in position L (82%) or position T (94%). Combined with the large scattering cross-section of the longitudinal resonance, this leads to the red emission coming almost exclusively from the longitudinal plasmonic dipole. Accordingly, the observed red emission will follow the polarization pattern of the longitudinal dipole, as confirmed by both experiment and simulation here and also in works by others^{58,60,61}.

In the case of coupling between the green-emitter and the transverse plasmonic dipole, we have to analyze the results in more detail because the polarization of the green-emission pattern is position-dependent. First, let us explore the efficiency of the FRET. As a result of the moderate overlap and smaller extinction cross-section, the calculated efficiency (the calculation is reproduced in full detail in the Supplementary Information) is now 31% for the green emitter in position L and 84% in position T. This tells us that the green emission will be composed of contributions from both the excited transverse plasmonic dipole and the bare emitters themselves. To clarify how

these two contributions affect the shape of the polarization patterns, Figure 7 shows the calculated charge distribution on the surface of a GNR@SiO₂ excited by a green-emission dipole in various positions. For the green-emission dipole in position L, when it is oriented parallel to the transverse axis of the GNR (Figure 7a), the induced charge distribution corresponds to a resonant transverse plasmonic dipole antiparallel to the green-emission dipole⁶². The radiative but antiparallel coherent charge oscillation will tend to be canceled out by the remaining part of the green-dipole emission that did not undergo FRET. In contrast, when the dipole is oriented parallel to the longitudinal axis of the GNR (Figure 7b), a non-resonant quadrupole charge distribution is induced in the GNR. The zero spectral overlap and dark nature of this mode jointly result in the negligible influence of the GNR on the UC emission in this configuration (this is consistent with the FRET theory, as the κ factor for this case is zero—see the discussion in Supplementary Information). Therefore, although the GNR itself does not act as a nanoantenna in this case, the destructive interference in the case of the other possible orientation leads to the plasmon-modulated green emission being polarized along the long axis of the GNR, as seen in the experiment and simulation. For the green-emission dipoles located in position T, the results are in many aspects analogous. When the green-emission dipole is oriented perpendicular to the transverse axis of the GNR (Figure 7c), a non-resonant quadrupole charge distribution is induced in the GNR again, leading to the UC emission being radiated to the far-field almost unperturbed. For a parallel-oriented green-emission dipole (Figure 7d), the induced charge distribution corresponds to a resonant plasmonic dipole, but—unlike in the previous case—with a

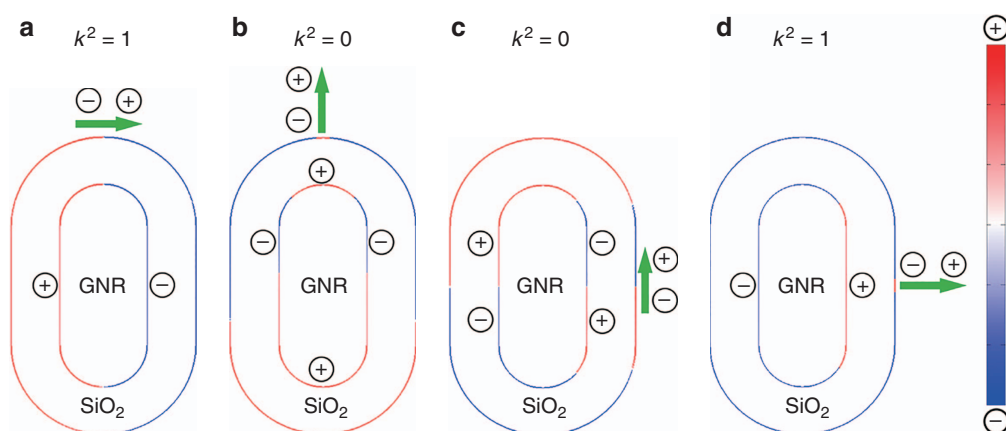


Figure 7 Calculated charge distribution on the surface of a GNR@SiO₂ excited by a green-emission dipole in position L (a, b) and position T (c, d). The dipoles are oriented either parallel a, d or perpendicular b, c to the orientation of the transverse plasmonic dipole of the GNR. Note that the green-emission dipole orientation is represented by enlarged black arrows and the nature of the induced charge configurations is labeled by +/− signs.

parallel rather than an antiparallel orientation⁶². This will lead to constructive interference with the remaining uncoupled part, and these dipoles will thus dominate the green-emission from position T, which will become polarized as the transverse dipole of the GNR.

To provide an even better visualization of the difference between the polarization patterns of green and red emissions from dipolar emitters at position T of a bare GNR (without a SiO₂ shell), we performed another set of finite-difference time-domain calculations to simulate the 3D emission patterns of a single dipolar source located in the vicinity of a bare GNR. The dipoles are set at a 45° angle to the long axis of the GNR to keep our discussion simple and at the same time to represent the real situation of the random-oriented dipoles of the UCNCs. The results of our simulations are summarized in Figure 8 for a set of distances between the dipole and the core of the GNR—covering a region between 20 and 100 nm. From the 3D emission patterns, one can clearly see that the emission pattern of a dipole in the close vicinity of a GNR becomes significantly warped as the GNR ‘imprints’ a polarized plasmon-scattered light into it, in sharp contrast to the well-known doughnut-shaped radiation pattern of a bare dipole source. In the case of the green-emission dipole, the emission pattern bends towards the Y axis as the FRET takes place, and the emission becomes modified by the transverse plasmonic dipole of the GNR (Figure 8a). When the distance between the dipole source and the GNR increases, the emission pattern returns back to the doughnut shape for a bare dipole as the modulation effect of the plasmonic dipole rapidly fades away. For the red emission dipole in the closest vicinity of the GNR, the FRET efficiency approaches 100%, and the emission pattern is dominated by the longitudinal dipole of the GNR (Figure 8b). This influence decreases much slowly owing to the larger Förster radius for the red emission (see the comparison of the calculated Förster radii for the GNR@SiO₂ nanostructure shown in Supplementary Table S2).

Because the plasmon-induced polarized UC emission can be observed only at the single-particle level, the emission intensity from one GNR@SiO₂@CaF₂:Yb³⁺,Er³⁺ hybrid nanostructure is very low, which limits its potential applications in real life. In the last section of this paper, we propose a template-assisted self-assembly method to obtain an intense polarized UC emission from an array of hybrid nanostructures. In this approach, a transparent glass substrate would be first patterned with a series of slots using electron-beam lithography to act as a template. The GNR@SiO₂@CaF₂:Yb³⁺,Er³⁺ hybrid

nanostructures could be assembled into the slots by a template-assisted self-assembly method reported by Kagan’s group^{25,31}. The shape of the slots should be precisely designed so that each slot could be occupied by only one hybrid nanostructure. Figure 9 shows the schematic of an array of GNR@SiO₂@CaF₂:Yb³⁺,Er³⁺ hybrid nanostructures assembled on a transparent glass template. When the polarization of the excitation laser is parallel to either the long or short axis of the hybrid nanostructure, this array structure could generate polarized UC emissions with strong intensity, and the polarization direction could be easily switched by excitation polarization. The proposed system can find wide applications ranging from illuminators in spectrometers to polarization-sensitive nanoscale photodetectors^{40,63}.

CONCLUSIONS

In summary, we developed a facile and effective method for the large-scale synthesis of hybrid GNR@SiO₂@CaF₂:Yb³⁺,Er³⁺ core-shell-satellite nanostructures. By the precise control of the thickness of the silica shell, the distance-dependent plasmon-enhanced UC luminescence was investigated. The highest UC emission enhancement was obtained for the shell thickness ~20 nm, and the enhancement factors reached 3 and 6.7 for the green and red emissions, respectively. Furthermore, we fully analyzed the polarization state of the UC emissions from a single hybrid nanostructure illuminated by an excitation laser with polarization parallel or perpendicular to the long axis of the GNR. Our results demonstrate the unusual polarized nature of the light at the two UC emission bands, which was dictated by the relationship between the excitation polarization and the GNR orientation, namely, that the polarization of the red emission is insensitive to the polarization state of the excitation laser, whereas the green emission follows the excitation polarization. Utilizing electrodynamic calculations and FRET theory, we analyzed the complicated relationship between the emission dipoles and plasmonic dipoles and elucidated how their orientations and mutual positions determine the polarization state of the UC emission in various situations. Our findings open a new method to control the UC emission polarization by introducing a plasmonic nanomaterial with a specific structure. Finally, our bioimaging experiments and proposed ordered plasmonic UC nanostructure arrays demonstrate that this technique can bring novel functions to UCNCs and is therefore relevant and advantageous for all applications based on their extraordinary properties.

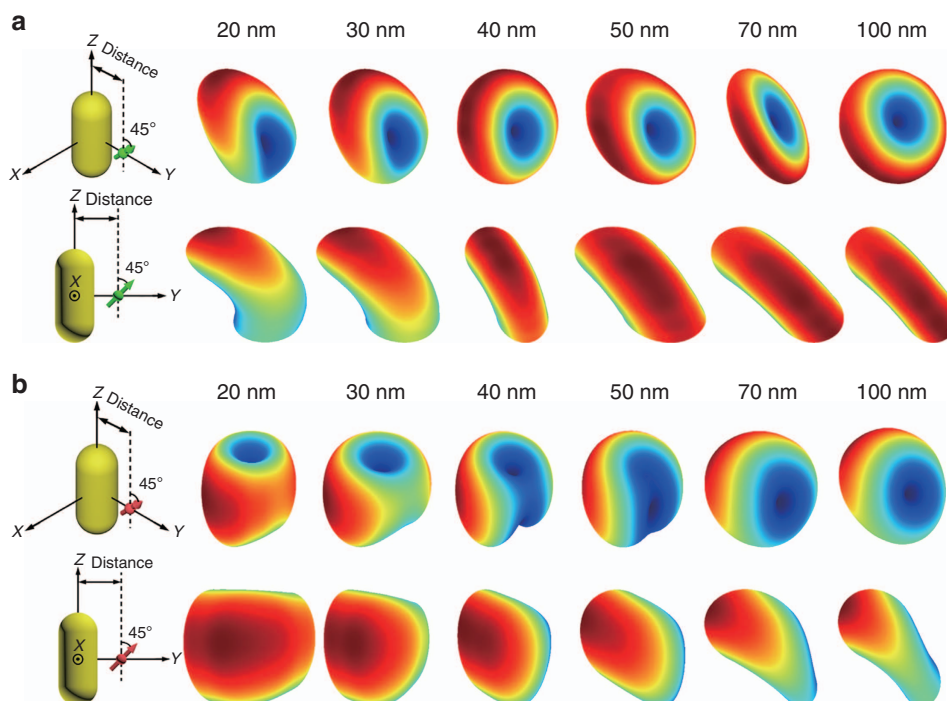


Figure 8 3D far-field-emission patterns of a dipole source in the vicinity of a bare GNR (diameter 32 nm, length 82 nm). The dipole is located in the Y - Z plane, and it is aligned at a 45° angle from the Z axis. The distance between the dipole and the center of the GNR is varied from 20 to 100 nm. The emission wavelength of the dipole was set to (a) 540 nm and (b) 660 nm. The first frame of each row indicates how the far-field-emission patterns are viewed.

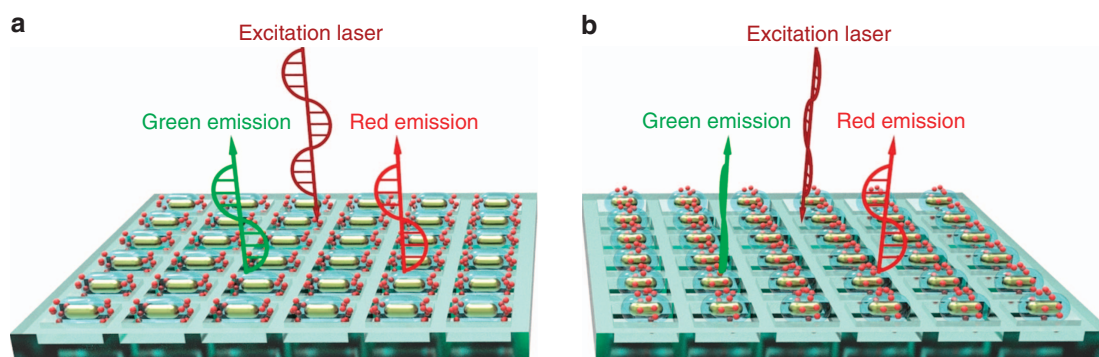


Figure 9 Schematic of ordered arrays of GNR@SiO₂@CaF₂:Yb³⁺,Er³⁺ hybrid nanostructure assembled on patterned templates. (a) When the polarization of the excitation laser (deep-red arrow) is parallel to the long axis of the hybrid nanostructures, both the enhanced green and red UC emissions (dictated by green and red arrows, respectively) would have the same polarization as the excitation laser. (b) In the case of the excitation laser with a perpendicular polarization, the resulting green UC emission would have the same polarization as the excitation laser, whereas the polarization of the red emission would be perpendicular to that of the green emission.

CONFLICT OF INTEREST

The authors declare no conflict of interest.

ACKNOWLEDGEMENTS

We acknowledge the financial support by the Hong Kong Research Grants Council (GRF Grant No. 15301414). FL acknowledges the support by the Ministry of Education, Youth and Sports of the Czech Republic under project CEITEC 2020 (LQ1601) and by the Hong Kong Polytechnic University. XC and WZ acknowledge the financial support by the NSFC (Nos. U1305244, 21325104, 11304314) and the CAS/SAFEA International Partnership Program for Creative Research Teams. JH thanks Mr. Gongxun Bai and Mr Ming-Kiu Tsang for assistance in using the Edinburgh FLS920 Fluorescence Spectrometer. JH also thanks Zijian Zheng and Xiaoling Wei for assistance in the zeta-potential measurements.

- 1 Wang F, Banerjee D, Liu YS, Chen XY, Liu XQ. Upconversion nanoparticles in biological labeling, imaging, and therapy. *Analyst* 2010; **135**: 1839–1854.
- 2 Liu YS, Tu DT, Zhu HM, Chen XY. Lanthanide-doped luminescent nanoprobes: controlled synthesis, optical spectroscopy, and bioapplications. *Chem Soc Rev* 2013; **42**: 6924–6958.
- 3 Chen GY, Qiu HL, Prasad PN, Chen XY. Upconversion nanoparticles: design, nanochemistry, and applications in theranostics. *Chem Rev* 2014; **114**: 5161–5214.
- 4 Zheng W, Tu DT, Huang P, Zhou SY, Chen Z *et al*. Time-resolved luminescent biosensing based on inorganic lanthanide-doped nanoprobes. *Chem Commun* 2015; **51**: 4129–4143.
- 5 Liu Q, Sun Y, Yang TS, Feng W, Li CG *et al*. Sub-10 nm hexagonal lanthanide-doped NaLuF₄ upconversion nanocrystals for sensitive bioimaging *in vivo*. *J Am Chem Soc* 2011; **133**: 17122–17125.
- 6 Cheng L, Yang K, Li YG, Chen JH, Wang C *et al*. Facile preparation of multifunctional upconversion nanoprobes for multimodal imaging and dual-targeted photothermal therapy. *Angew Chem Int Ed* 2011; **50**: 7385–7390.
- 7 Yang JP, Shen DK, Zhou L, Li W, Fan JW *et al*. Mesoporous silica-coated plasmonic nanostructures for surface-enhanced Raman scattering detection and photothermal therapy. *Adv Healthc Mater* 2014; **3**: 1620–1628.

- 8 Wang HQ, Batentschuk M, Osvet A, Pinna L, Brabec CJ. Rare-earth ion doped up-conversion materials for photovoltaic applications. *Adv Mater* 2011; **23**: 2675–2680.
- 9 Yu DC, Martín-Rodríguez R, Zhang QY, Meijerink A, Rabouw FT. Multi-photon quantum cutting in $\text{Gd}_2\text{O}_3\text{:Tm}^{3+}$ to enhance the photo-response of solar cells. *Light Sci Appl* 2015; **4**: e344, doi:10.1038/lsa.2015.117.
- 10 Auzel F. Upconversion and anti-stokes processes with f and d ions in solids. *Chem Rev* 2004; **104**: 139–174.
- 11 Boyer JC, van Veggel FCJM. Absolute quantum yield measurements of colloidal $\text{NaYF}_4\text{:Er}^{3+}, \text{Yb}^{3+}$ upconverting nanoparticles. *Nanoscale* 2010; **2**: 1417–1419.
- 12 Hao JH, Zhang Y, Wei XH. Electric-induced enhancement and modulation of upconversion photoluminescence in epitaxial $\text{BaTiO}_3\text{:Yb/Er}$ thin films. *Angew Chem Int Ed* 2011; **50**: 6876–6880.
- 13 Wang HQ, Nann T. Monodisperse upconverting nanocrystals by microwave-assisted synthesis. *ACS Nano* 2009; **3**: 3804–3808.
- 14 Liu YS, Tu DT, Zhu HM, Li RF, Luo WQ *et al*. A strategy to achieve efficient dual-mode luminescence of Eu^{3+} in lanthanides doped multifunctional NaGdF_4 nanocrystals. *Adv Mater* 2010; **22**: 3266–3271.
- 15 Chen GY, Ohulchanskyy TY, Liu S, Law WC, Wu F *et al*. Core/shell $\text{NaGdF}_4\text{:Nd}^{3+}/\text{NaGdF}_4$ nanocrystals with efficient near-infrared to near-infrared downconversion photoluminescence for bioimaging applications. *ACS Nano* 2012; **6**: 2969–2977.
- 16 Zhou B, Tao LL, Tsang YH, Jin W. Core-shell nanoarchitecture: a strategy to significantly enhance white-light upconversion of lanthanide-doped nanoparticles. *J Mater Chem C* 2013; **1**: 4313–4318.
- 17 Wang F, Wang J, Liu XG. Direct evidence of a surface quenching effect on size-dependent luminescence of upconversion nanoparticles. *Angew Chem Int Ed* 2010; **49**: 7456–7460.
- 18 Zhao JB, Jin DY, Scharfner EP, Lu YQ, Liu YJ *et al*. Single-nanocrystal sensitivity achieved by enhanced upconversion luminescence. *Nat Nanotechnol* 2013; **8**: 729–734.
- 19 Wang F, Deng RR, Wang J, Wang QX, Han Y *et al*. Tuning upconversion through energy migration in core-shell nanoparticles. *Nat Mater* 2011; **10**: 968–973.
- 20 Wang J, Wang F, Wang C, Liu Z, Liu XG. Single-band upconversion emission in lanthanide-doped KLnF_6 nanocrystals. *Angew Chem Int Ed* 2011; **50**: 10369–10372.
- 21 Han SY, Deng RR, Xie XJ, Liu XG. Enhancing luminescence in lanthanide-doped upconversion nanoparticles. *Angew Chem Int Ed* 2014; **53**: 11702–11715.
- 22 Zhang H, Li YJ, Ivanov IA, Qu YQ, Huang Y *et al*. Plasmonic modulation of the upconversion fluorescence in $\text{NaYF}_4\text{:Yb/Tm}$ hexaplate nanocrystals using gold nanoparticles or nanoshells. *Angew Chem Int Ed* 2010; **49**: 2865–2868.
- 23 Zhang F, Braun GB, Shi YF, Zhang YC, Sun XH *et al*. Fabrication of $\text{Ag}@\text{SiO}_2\text{:Y}_2\text{O}_3\text{:Er}$ nanostructures for bioimaging: tuning of the upconversion fluorescence with silver nanoparticles. *J Am Chem Soc* 2010; **132**: 2850–2851.
- 24 Schietinger S, Aichele T, Wang HQ, Nann T, Benson O. Plasmon-enhanced upconversion in single $\text{NaYF}_4\text{:Yb}^{3+}/\text{Er}^{3+}$ codoped nanocrystals. *Nano Lett* 2010; **10**: 134–138.
- 25 Saboktakin M, Ye XC, Chettiar UK, Engheta N, Murray CB *et al*. Plasmonic enhancement of nanophosphor upconversion luminescence in Au nanohole arrays. *ACS Nano* 2013; **7**: 7186–7192.
- 26 Wu DM, García-Etxarri A, Salleo A, Dionne JA. Plasmon-enhanced upconversion. *J Phys Chem Lett* 2014; **5**: 4020–4031.
- 27 Lu DW, Cho SK, Ahn S, Brun L, Summers CJ *et al*. Plasmon enhancement mechanism for the upconversion processes in $\text{NaYF}_4\text{:Yb}^{3+}, \text{Er}^{3+}$ nanoparticles: Maxwell versus Förster. *ACS Nano* 2014; **8**: 7780–7792.
- 28 Sun QC, Mundoor H, Ribot JC, Singh V, Smalyukh II *et al*. Plasmon-enhanced energy transfer for improved upconversion of infrared radiation in doped-lanthanide nanocrystals. *Nano Lett* 2014; **14**: 101–106.
- 29 Liu N, Qin WP, Qin GS, Jiang T, Zhao D. Highly plasmon-enhanced upconversion emissions from $\text{Au}@\beta\text{-NaYF}_4\text{:Yb, Tm}$ hybrid nanostructures. *Chem Commun* 2011; **47**: 7671–7673.
- 30 Priyam A, Idris NM, Zhang Y. Gold nanoshell coated NaYF_4 nanoparticles for simultaneously enhanced upconversion fluorescence and darkfield imaging. *J Mater Chem* 2012; **22**: 960–965.
- 31 Greybush NJ, Saboktakin M, Ye XC, Della Giovampola C, Oh SJ *et al*. Plasmon-enhanced upconversion luminescence in single nanophosphor-nanorod heterodimers formed through template-assisted self-assembly. *ACS Nano* 2014; **8**: 9482–9491.
- 32 Ge W, Zhang XR, Liu M, Lei ZW, Knize RJ *et al*. Distance dependence of gold-enhanced upconversion luminescence in $\text{Au/SiO}_2\text{:Y}_2\text{O}_3\text{:Yb}^{3+}, \text{Er}^{3+}$ nanoparticles. *Theranostics* 2013; **3**: 282–288.
- 33 Xu W, Min XL, Chen X, Zhu YS, Zhou PW *et al*. $\text{Ag-SiO}_2\text{-Er}_2\text{O}_3$ nanocomposites: highly effective upconversion luminescence at high power excitation and high temperature. *Sci Rep* 2014; **4**: 5087.
- 34 Chen GY, Agren H, Ohulchanskyy TY, Prasad PN. Light upconverting core-shell nanostructures: nanophotonic control for emerging applications. *Chem Soc Rev* 2015; **44**: 1680–1713.
- 35 Ming T, Chen HJ, Jiang RB, Li Q, Wang JF. Plasmon-controlled fluorescence: beyond the intensity enhancement. *J Phys Chem Lett* 2012; **3**: 191–202.
- 36 Yuan PY, Lee YH, Gnanasamandhan MK, Guan ZP, Zhang Y *et al*. Plasmon enhanced upconversion luminescence of $\text{NaYF}_4\text{:Yb, Er}@\text{SiO}_2\text{:Ag}$ core-shell nanocomposites for cell imaging. *Nanoscale* 2012; **4**: 5132–5137.
- 37 Liu X, Lei DY. Simultaneous excitation and emission enhancements in upconversion luminescence using plasmonic double-resonant gold nanorods. *Sci Rep* 2015; **5**: 15235.
- 38 Taminiau TH, Stefani FD, Segerink FB, van Hulst NF. Optical antennas direct single-molecule emission. *Nat Photonics* 2008; **2**: 234–237.
- 39 Chen P, Song M, Wu E, Wu BT, Zhou JJ *et al*. Polarization modulated upconversion luminescence: single particle vs. few-particle aggregates. *Nanoscale* 2015; **7**: 6462–6466.
- 40 Zhou JJ, Chen GX, Wu E, Bi G, Wu BT *et al*. Ultrasensitive polarized up-conversion of $\text{Tm}^{3+}\text{-Yb}^{3+}$ doped $\beta\text{-NaYF}_4$ single nanorod. *Nano Lett* 2013; **13**: 2241–2246.
- 41 Singh A, Calbris G, van Hulst NF. Vectorial nanoscale mapping of optical antenna fields by single molecule dipoles. *Nano Lett* 2014; **14**: 4715–4723.
- 42 Tuchin VV, Wang LH, Zimnyakov DA. *Optical Polarization in Biomedical Applications*. Berlin/Heidelberg: Springer; 2006.
- 43 Tuchin V. *Tissue Optics: Light Scattering Methods and Instruments for Medical Diagnosis*, 2nd edn. Bellingham, WA, USA: SPIE Publications; 2007.
- 44 Ming T, Zhao L, Yang Z, Chen HJ, Sun LD *et al*. Strong polarization dependence of plasmon-enhanced fluorescence on single gold nanorods. *Nano Lett* 2009; **9**: 3896–3903.
- 45 Gorelikov I, Matsuura N. Single-step coating of mesoporous silica on cetyltrimethyl ammonium bromide-capped nanoparticles. *Nano Lett* 2008; **8**: 369–373.
- 46 He JJ, Zheng W, Chen XY, Lei DY. Plasmon-modulated polarized upconversion emissions from single gold nanorod-nanophosphors hybrid nanostructures. In: *International Photonics and Optoelectronics*. Washington, DC, USA: OSA; 2015.
- 47 Zheng W, Zhou SY, Chen Z, Hu P, Liu YS *et al*. Sub-10 nm lanthanide-doped CaF_2 nanoprobes for time-resolved luminescent biodetection. *Angew Chem Int Ed* 2013; **52**: 6671–6676.
- 48 Huang P, Zheng W, Zhou SY, Tu DT, Chen Z *et al*. Lanthanide-doped LiLuF_4 upconversion nanoprobes for the detection of disease biomarkers. *Angew Chem Int Ed* 2014; **53**: 1252–1257.
- 49 Bao ZY, Lei DY, Jiang RB, Liu X, Dai JY *et al*. Bifunctional $\text{Au}@\text{Pt}$ core-shell nanostructures for in situ monitoring of catalytic reactions by surface-enhanced Raman scattering spectroscopy. *Nanoscale* 2014; **6**: 9063–9070.
- 50 Li N, Tittel A, Yue S, Giessen H, Song C *et al*. DNA-assembled bimetallic plasmonic nanosensors. *Light Sci Appl* 2014; **3**: e226, doi:10.1038/lsa.2014.107.
- 51 Chen HJ, Shao L, Li Q, Wang JF. Gold nanorods and their plasmonic properties. *Chem Soc Rev* 2013; **42**: 2679–2724.
- 52 Bogdan N, Vetrone F, Ozin GA, Capobianco JA. Synthesis of ligand-free colloidal stable water dispersible brightly luminescent lanthanide-doped upconverting nanoparticles. *Nano Lett* 2011; **11**: 835–840.
- 53 Zhang ZJ, Wang LM, Wang J, Jiang XM, Li XH *et al*. Mesoporous silica-coated gold nanorods as a light-mediated multifunctional theranostic platform for cancer treatment. *Adv Mater* 2012; **24**: 1418–1423.
- 54 Li ZQ, Wang LM, Wang ZY, Liu XH, Xiong YJ. Modification of $\text{NaYF}_4\text{:Yb, Er}@\text{SiO}_2$ nanoparticles with gold nanocrystals for tunable green-to-red upconversion emissions. *J Phys Chem C* 2011; **115**: 3291–3296.
- 55 Abadeer NS, Brennan MR, Wilson WL, Murphy CJ. Distance and plasmon wavelength dependent fluorescence of molecules bound to silica-coated gold nanorods. *ACS Nano* 2014; **8**: 8392–8406.
- 56 Huang YJ, Kim DH. Dark-field microscopy studies of polarization-dependent plasmonic resonance of single gold nanorods: rainbow nanoparticles. *Nanoscale* 2011; **3**: 3228–3232.
- 57 Li GC, Zhang YL, Lei DY. Hybrid plasmonic gap modes in metal film-coupled dimers and their physical origins revealed by polarization resolved dark field spectroscopy. *Nanoscale* 2016; **8**: 7119–7126.
- 58 Ming T, Zhao L, Chen HJ, Woo KC, Wang JF *et al*. Experimental evidence of plasmaphores: plasmon-directed polarized emission from gold nanorod-fluorophore hybrid nanostructures. *Nano Lett* 2011; **11**: 2296–2303.
- 59 Reifengerger JG, Snyder GE, Baym G, Selvin PR. Emission polarization of europium and terbium chelates. *J Phys Chem B* 2003; **107**: 12862–12873.
- 60 Curto AG, Taminiau TH, Volpe G, Kreuzer MP, Quidant R *et al*. Multipolar radiation of quantum emitters with nanowire optical antennas. *Nat Commun* 2013; **4**: 1750.
- 61 Sugimoto H, Chen TH, Wang R, Fujii M, Reinhard BM *et al*. Plasmon-enhanced emission rate of silicon nanocrystals in gold nanorod composites. *ACS Photonics* 2015; **2**: 1298–1305.
- 62 Fischer S, Hallermann F, Eichelkraut T, von Plessen G, Krämer KW *et al*. Plasmon enhanced upconversion luminescence near gold nanoparticles—simulation and analysis of the interactions: errata. *Opt Express* 2013; **21**: 10606–10611.
- 63 Ren MX, Chen M, Wu W, Zhang LH, Liu JK *et al*. Linearly polarized light emission from quantum dots with plasmonic nanoantenna arrays. *Nano Lett* 2015; **15**: 2951–2957.



This work is licensed under a Creative Commons Attribution-NonCommercial-ShareAlike 4.0 International License. The images or other third party material in this article are included in the article's Creative Commons license, unless indicated otherwise in the credit line; if the material is not included under the Creative Commons license, users will need to obtain permission from the license holder to reproduce the material. To view a copy of this license, visit <http://creativecommons.org/licenses/by-nc-sa/4.0/>

© The Author(s) 2017

Supplementary Information for this article can be found on the *Light: Science & Applications*' website (<http://www.nature.com/lsa>).